Research Square

Preprints are preliminary reports that have not undergone peer review.
They should not be considered conclusive, used to inform clinical practice,
or referenced by the media as validated information.

Screen-Printed Carbon/TiO_2 Counter Electrodes for Indoor Dye-Sensitized Solar Cells Using TiO_2 - Inorganic Binders Prepared via Polyvinylpyrrolidone-Assisted Sol-Gel Synthesis

Tatiana Buchlová
Slovak University of Technology in Bratislava
Michal Hatala
4D – National Research Centre for Defense and Dual Technologies of the University of Ss. Cyril and Methodius in Trnava
Izabela Vajová
Slovak University of Technology in Bratislava
Roberto Speranza
Politecnico di Torino
Andrea Lamberti
Politecnico di Torino
Pavol Gemeiner
pavol.gemeiner@stuba.sk

Slovak University of Technology in Bratislava

Article

Keywords: Dye-sensitized solar cells, Counter-electrodes, Carbon/TiO2 composites, sol-gel, Screen-printing, indoor photovoltaics

Posted Date: August 27th, 2026

DOI: https://doi.org/10.21203/rs.3.rs-10680459/v1

License: This work is licensed under a Creative Commons Attribution 4.0 International License.
Read Full License

Additional Declarations: No competing interests reported.

Abstract

Dye-sensitized solar cells (DSSCs) represent a promising technology for indoor energy harvesting owing to their high performance under low-intensity light and compatibility with low-cost coating and printing techniques. Carbon-based counter electrodes (CEs) offer an affordable Pt-free alternative for DSSCs, yet screen-printed carbon electrodes often contain organic binders such as ethyl cellulose (EC), which can hinder charge transport and electrolyte access to active sites. In this work, PVP-assisted sol–gel TiO_2 inorganic binders (SG) were investigated as alternatives to EC in carbon black/graphite (CB.G) inks for screen-printed CEs. The binders were synthesized from titanium isopropoxide (20 wt.%) in ethylene glycol with acetic acid (7 wt.%), while the PVP content was varied from 0.5 to 3 wt.% (SG0.5-SG3) to adjust the rheological behaviour and printability. All CB.G/SG inks exhibited flow behaviour suitable for screen-printing, and higher PVP content improved printed pattern definition, enabling a minimum resolved line width of 200 µm. After sintering at 480°C, Raman spectroscopy confirmed the anatase TiO_2 within the composite CEs, with crystallite sizes of 11–17 nm. Compared with the EC-based reference, the carbon/TiO_2 CEs exhibited improved mechanical stability, lower sheet resistance and more effective charge transfer at the interface between CE and I^-/I_3^- electrolyte. Among the studied composite CEs, CB.G/SG2.5, prepared using a TiO_2-based binder containing 2.5 wt. % PVP, showed the most favourable balance between adhesion to the FTO substrate, sheet resistance (149 Ω/sq) and charge-transfer resistance (20.01 $\Omega.cm^2$). When implemented in DSSCs under LED indoor illumination, the CB.G/SG2.5 CE led to PCEs of 18.94% at 1000 lux and 15.41% at 200 lux, exceeding the corresponding Pt-based reference values of 18.11% and 14.34%, respectively. These results demonstrate the potential of PVP-stabilized TiO_2 inorganic binders as EC alternatives for screen-printed carbon-based CEs in indoor DSSCs.

Introduction

The rapid expansion of wireless electronics and Internet of Things (IoT) devices has increased the demand for sustainable power sources operating under indoor illumination. Among emerging photovoltaic technologies, dye-sensitized solar cells (DSSCs) have attracted considerable attention owing to their efficient conversion of diffuse artificial light, with reported indoor power conversion efficiencies (PCEs) reaching 38%[1]. Together with their potential for flexible and semi-transparent designs and compatibility with low-cost coating and printing techniques, these features make DSSCs promising candidates for powering autonomous sensors, portable electronics and wireless monitoring systems[2–4]. Their integration with supercapacitors may further provide a more sustainable alternative to conventional battery-based power supplies[5]. In standard DSSCs employing the ruthenium dye N719 and the iodide/triiodide (I^-/I_3^-) electrolyte, platinum is commonly used as the catalytically active counter electrode (CE) material for I_3^- reduction. The high cost of Pt and susceptibility to corrosion in the electrolyte environment, are one of the main drawbacks limiting the broader commercialization of DSSCs[6–8].

Carbon materials, such as graphite, carbon black, carbon nanotubes, graphene, graphene oxide and biochar, have been intensively investigated as promising alternatives to Pt[9–11]. In general, carbon-based CEs are characterized by low fabrication cost, chemical stability in the electrolyte environment, suitable electrical conductivity and a porous structure providing a large specific surface area[12,13]. Among them, the combination of graphite and carbon black represents a widely used and cost-effective choice for carbon-based CEs. Graphite provides conductive pathways for electron transport, while nanospherical carbon black particles fill the spaces between larger graphite flakes, improve interparticle contact and increase the accessible electrochemically active surface area of the CE[14,15]. Moreover, carbon-based CEs are compatible with electrolytes based on copper and cobalt complexes, which are widely studied for indoor DSSC applications[16–18]. Their electrical and catalytic properties can be further improved by combination with metal oxides, metal sulfides or conducting polymers[19–21]. In this context, one of the highest reported PCEs for DSSCs employing carbon-based composite CEs under indoor illumination is 25.17 % at 1000 lux, achievedusing a poly(3,4-ethylenedioxythiophene) (PEDOT)/carbon black catalytic layer combined with a TiO_2/Y123 photoanode and a Cu(II/I)-mediated electrolyte[22]. Among oxide components, SnO_2, TiO_2 and SiO_2 have been investigated in carbon-based CEs, mainly affecting layer microstructure, adhesion to FTO and charge-transfer resistance at the CE/electrolyte interface[23–26].

Screen printing is a widely used, simple and low-cost technique for the fabrication of carbon-based CEs with defined geometry. However, the quality of the printed layer strongly depends on the rheological behaviour of the dispersion, particularly its shear-thinning character and thixotropy, which enable flow through the screen mesh followed by shape retention after printing [27,28]. Therefore, organic polymer binders such as ethyl cellulose are commonly used in highly viscous carbon dispersions to provide adhesion to the substrate, particle cohesion and suitable rheological properties. However, their insulating nature can hinder charge transport and electrolyte access to active sites, thereby increasing layer resistance and reducing CE catalytic activity and DSSC efficiency[12,29].

Inorganic binders based on titanium dioxide (TiO_2) prepared via the sol–gel method represent a promising alternative to organic polymer binder systems. During sol–gel synthesis, titanium alkoxides undergo hydrolysis and condensation in an alcohol-based solvent, forming a titanium–oxide polymeric network from which anatase TiO_2 nanoparticles can be obtained after heat treatment[30,31]. In a carbon catalytic layer, TiO_2 can act as an inorganic binder, ensuring interparticle contact, adhesion to the substrate and more efficient charge transport within the CE. This approach has been partially investigated in composite carbon CEs for DSSCs containing carbon black, graphite and titanium isopropoxide (TTIP). TiO_2 formed during sintering at 500°C contributed to improved structural and electrochemical properties of the CE, while its presence in the carbon layer increased the DSSC efficiency under standard illumination (100 $mW.cm^{-2}$) from 3.67 % to5.74 %[32]. Te binding function of TiO_2 prepared from TTIP was also confirmed in our previous work, where its presence in a screen-printed biochar-based CE improved mechanical stability and reduced the charge-transfer resistance at the CE/electrolyte interface[33]. However, the rheological properties and printability of the dispersions

remained limited, highlighting the need for further optimisation of the inorganic binder composition. Accordingly, the stability of the sol–gel system and TiO_2 nanoparticle formation are mainly governed by the precursor type and concentration, pH and solvent[34–36]. Polymer additives, such as polyvinylpyrrolidone (PVP), play an important role, as they affect hydrolysis and condensation, stabilization of the resulting system and the flow behaviour of the sol–gel system[37–39]. TiO_2 sol–gel systems containing PVP have been used in applications such as DSSC photoanodes, biosensors, gas sensors and photocatalytic materials[40–44]. However, the role of PVP in TiO_2 inorganic binder formulations for screen-printed carbon CEs remains to be thoroughly investigated.

Here, we present the systematic preparation of TiO_2 inorganic binders by sol–gel synthesis as an alternative to standard polymeric binder ethyl cellulose in screen-printable carbon black/graphite inks for DSSC CEs. TTIP and ethylene glycol were used as the TiO_2 precursor and solvent, respectively, while the PVP concentration was varied to stabilize the sol–gel system and adjust its flow behaviour. The prepared formulations allowed the development of shear-thinning carbon/TiO_2 inks with suitable behaviour for screen printing, while higher PVP contents improved printability. After sintering, anatase TiO_2 nanoparticles were formed within the composite layers, contributing to enhanced cohesion, adhesion to FTO and lower sheet resistance compared with the ethyl cellulose-based reference. The optimized composite CE showed favourable electrochemical properties, resulting in DSSC efficiencies of 18.94% at 1000 lux and 15.41% at 200 lux under indoor illumination. Overall, the results demonstrate the suitability of PVP-stabilized TiO_2 inorganic binders for the fabrication of low-cost, printable carbon-based CEs for indoor DSSC applications.

Experimental

Sol-gel synthesis of titania-based inorganic binders with polyvinylpyrrolidone additive

In the first step, the initial binder system was prepared by dissolving 0.5–3 wt.% polyvinylpyrrolidone (PVP, $M_W = 360 \times 10^3$ g/mol, Sigma Aldrich) in a solution of ethylene glycol (EG) (ReagentPlus, ≥ 99%, Merck, Germany) at 48°C. Acetic acid (AcOH, w = 7 wt.%) (glacial, EMSURE, Supelco, Merck, Germany) was gradually added under constant stirring. Subsequently, 20 wt.% of the titanium dioxide nanoparticles precursor, titanium(IV) isopropoxide (TTIP) (≥ 97.0%, Merck, Germany) was introduced at a controlled rate of 250 $\mu L.min^{-1}$ with the dosing needle immersed in the solution to prevent air exposure, while yellow coloration was observed, indicating hydrolytic reactions. After 3 hours of continuous stirring, the solutions were aged for 48 hours in the dark under low humidity to allow condensation and the formation of the TiO_2 network, as evidenced by gelation and white turbidity. The compositions of the prepared inorganic binders are summarized in Table 1, where they are labelled as SG0.5–3 according to PVP content. In addition to binders containing 20 wt.% of TTIP, analogous binders with 30 wt.% of TTIP were

prepared at varying PVP concentrations. However, higher precursor content resulted in highly viscous gels unsuitable for further preparation of screen-printing carbon-based inks.

Table 1
Chemical composition of inorganic binders containing TiO_2

Inorganic binder	TTIP (wt.%)	AcOH (wt.%)	PVP (wt.%)	EG (wt.%)
SG0.5	20	7	0.5	72.5
SG1	20	7	1.0	72.0
SG1.5	20	7	1.5	71.5
SG2	20	7	2.0	71.0
SG2.5	20	7	2.5	70.5
SG3	20	7	3.0	70.0

Preparation of carbon-based inks with titania-based inorganic binders

Inorganic binders containing 20 wt.% of TTIP, serving as a TiO_2 nanoparticle precursor in EG and varying PVP content were used for preparation of high-viscosity inks based on 20 wt.% of carbon black (CB) (ENSACO 250G, IMERYS, Belgium) and graphite (G) (graphite powder, particle size ≤ 20 µm, Merck, Germany) in a 1:3 ratio, selected based on our previous study[45]. Homogenization process was carried out for 5 minutes using a hand-held mixing unit equipped with a cylindrical steel container and a stainless roller stirrer, while maintaining ambient cooling at 15°C to prevent overheating caused by high shear forces. To adjust the rheological properties of the carbon dispersions for the screen-printing technique, an additional 10 wt.% ethylene glycol was added, followed by further homogenization for 3 min. The prepared screen-printing carbon inks with inorganic binders were denoted CB.G/SG0.5, CB.G/SG1, CB.G/SG1.5, CB.G/SG2, CB.G/SG2.5, CB.G/SG3, reflecting the PVP content in the binder. For comparison, a reference dispersion based on CB and G (20 wt.%) in a 1:3 ratio and an ethyl cellulose binder (CB.G/EC) was prepared using the same procedure. The binder was obtained by dissolving 10 wt.% ethyl cellulose (EC) (viscosity 22 cP, Merck, Germany) in diethylene glycol butyl ether (DEGBE) (≥ 99 % bp 231°C, Merck, Germany) at 90°C under continuous stirring.

Preparation of counter electrodes

For counter electrodes preparation, glass substrates (15 × 20 mm, thickness 2.2 mm) coated with a transparent conductive fluorine-doped tin oxide layer (FTO,7 Ω/sq; TEC, Ossila, United Kingdom) were used. The substrates were sequentially cleaned in an aqueous detergent solution, acetone, and isopropyl

alcohol in an ultrasonic cleaner (Kraintek, Czech Republic), with each step lasting 20 min. Subsequently, they were exposed to UV–O_3 radiation for 15 min to eliminate residual organic contaminants. CB.G/SG inks containing 20 wt.% carbon black and graphite (1:3), 20 wt.% TTIP, and 0.5–3 wt.% PVP in inorganic binders, as well as the CB.G/EC reference ink incorporating ethyl cellulose as the organic binder, were screen-printed onto the pre-drilled FTO substrates. For the screen-printing process, a manual screen-printing device (P65–80 kN, Drucktech, Hungary) with a polyester mesh stencil (71 threads/cm, 48 μm fiber diameter; PME 71–48 Y, SEFAR) was used. After printing, the wet screen-printed layers (0.6 × 0.6 cm) were left under laboratory conditions for 10 min to allow levelling and were then dried in a hot-air oven at 150°C for 15 min. Finally, the CEs were sintered in a muffle furnace at 480°C for 45 min. The reference platinum CE, commonly used in DSSCs, was prepared by doctor-blade coating on an FTO substrate using a transparent high-viscosity platinum-precursor ink (Platisol T/SP, Solaronix, Switzerland), followed by sintering at 450°C for 20 min.

DSSC fabrication

Photoanodes were fabricated according to the procedure reported in our previous study[33]. A transparent mesoporous TiO_2 photoactive layer (0.5 × 0.5 cm) was screen-printed using a commercial paste with 25 nm TiO_2 nanoparticles (Ti-Nanoxide T/SP, Solaronix, Switzerland). A scattering TiO_2 layer was deposited from a commercial paste containing 180 nm TiO_2 nanoparticles (Ti-Nanoxide R/SP, Solaronix). The photoanodes were sensitized for 16 hours in a 5 mM solution of ruthenium dye Ruthenizer 535-bis-TBA (N719, cis-bis(isothiocyanato)bis(2.2-bipyridil-4.4-dicarboxylato)-ruteniumII, Solaronix) in absolute ethanol with 50 mM of chenodeoxycholic acid (CDCA, Solaronix).

DSSCs were assembled by thermal sealing of the photoanode and counter electrode using a 60 μm thick thermoplastic sealing foil (Meltonix 117 − 60, Solaronix) with outer dimensions of 13 × 13 mm and an inner opening of 9 × 9 mm. The DSSCs were filled with a liquid electrolyte containing I^-/I_3^- redox pair (Iodolyt HI-30, Solaronix) through a pre-drilled hole (d = 0.5 mm) on the counter-electrode side using a Vac'n'Fill Syringe (Solaronix), followed by sealing of the filling hole.

Measurements and characterisation

Rheological properties of TiO_2-based inorganic binders and corresponding screen-printing carbon-based inks with inorganic binders (CB.G/SG0.5–3) were characterized using a rotational rheometer (HAAKE MARS iQ, Thermo Fisher Scientific) equipped with a parallel-plate geometry (d = 35 mm, gap height 0.5 mm) at a constant temperature of 25°C. Shear stress and dynamic viscosity of inorganic binders and inks were determined as a function of applied shear rate from 0.1 s^{-1} to 100 s^{-1}. The structural breakdown and viscosity recovery relevant to the screen-printing process were studied by the three-interval thixotropy test (3ITT), consisting of the shear-rate segments: 0.1 s^{-1} for 180 s, 100 s^{-1} for 30 s, and 0.1 s^{-1} for 600 s. The viscosity recovery was expressed as the percentage ratio between the

viscosity values obtained in the initial and final intervals. Printability of inks containing CB and G was further investigated by screen-printing of patterned layers with line widths of 150—500 µm onto a glass substrate under the same conditions used for the CEs preparation. The widths of the resulting interdigital structures were analysed with an optical microscope Leica DM6 M (Leica Microsystems, Germany). Raman spectra of the screen-printed electrodes (CB.G/SG0.5–3) were recorded using a DXR™ 3xi Raman Imaging Microscope (Thermo Scientific™, USA) with a 532 nm excitation laser. The size of TiO_2 nanoparticles formed in the presence of carbon particles was estimated from the position and full width at half maximum (FWHM) of the Eg vibration mode[46]. For comparison, TiO_2 layers without carbon were prepared by screen printing inorganic binders (SG0.5–3) with varying PVP content onto FTO substrates under the same conditions as used for the preparation of CB.G/SG electrodes. The surface morphology and microstructure of the screen-printed composite carbon/TiO_2 layers, together with their Ti distribution and surface homogeneity, were examined by scanning electron microscopy coupled with energy-dispersive X-ray spectroscopy (SEM/EDS) using a JSM-IT500HR InTouchScope™ microscope (JEOL, Japan). The measurements were carried out at an acceleration voltage of 15 kV, a working distance of 10 mm, and magnifications of × 2,500 and × 50,000. Mechanical stability of the sintered screen-printed composite carbon/TiO_2 electrodes was examined by an adhesive tape test using ISO 2409 / ISO 8502-3 adhesive tape (Elcometer, UK) applied under a constant load ensured by a 420 g roller. The tape was subsequently removed at a 180° angle. Optical density was measured using a reflective densitometer (TECHKON, Germany). The measurements were performed on adhesive tape containing residues of the detached layer, placed on a white substrate serving as the background. The final optical density represents the average value of ten measurements taken across the sample[45]. The sheet resistance (R_{sh}) of composite carbon/TiO_2 layers (CB.G/SG0.5-3) deposited on a glass substrate by screen-printing was determined using the device Four-Point Probe System (Ossila, UK). The reported sheet resistance values represent the average of twenty measurements collected from two parallel samples. The electrochemical activity of the screen-printed carbon/TiO_2 electrodes (CB.G/SG0.5–3), the carbon-based electrode (CB.G/EC), and the Pt electrode used in standard DSSC configuration was studied by cyclic voltammetry (CV) using a potentiostat/galvanostat PalmSens4 (PalmSens, NL). Measurements were carried out in a three-electrode system with the tested electrode serving as the working electrode, Ag/AgCl (3 M KCl) as the reference electrode, and Pt wire as the counter electrode. The acetonitrile electrolyte consisted of 0.1 M $LiClO_4$, 10 mM LiI, and 1.1 mM I_2. Cyclic voltammograms were recorded over the potential range from − 0.5 V to 1.0 V at a scan rate of 100 $mV.s^{-1}$ for 30 cycles. The electrochemical impedance spectroscopy (EIS) was employed to characterize symmetrical dummy cells filled with I^-/I_3^- electrolyte (Iodolyt HI-30, Solaronix) using a potentiostat/galvanostat PalmSens4 (PalmSens, NL). The measurements were performed over a frequency range of 10^{-1}—10^5 Hz with an AC amplitude of 10 mV. Dye-sensitized solar cells (DSSCs) with an active photoanode area of 25 mm^2 were characterized by photovoltaic measurements using a device Solar Cell I–V Test System (Ossila, UK). The measurements were performed under standard simulated solar irradiation (100 $mW.cm^{-2}$, AM 1.5G) and under indoor illumination of 1000 lux (313 $\mu W.cm^{-2}$) and 200 lux (63 $\mu W.cm^{-2}$), provided by an LED

Solar Simulator (Ossila, UK) equipped with an Indoor Light Simulation Filter (Ossila, UK) placed inside a black box.

Results and discussion

Properties of inorganic binders and carbon-based screen-printing inks CB.G/SG

Shear-thinning behaviour is a key requirement for screen-printing technology, as it determines the ink's ability to flow effectively through the mesh under applied shear[28]. Therefore, the rheological properties of the prepared sol–gel-derived TiO_2-based gels containing 20 wt.% of titanium isopropoxide (TTIP) and polyvinylpyrrolidone (PVP) in the range of 0.5–3 wt.% (SG0.5–SG3) were first investigated in terms of their flow behaviour and structural stability, with the aim of their application as inorganic binders in the preparation of carbon dispersions. The dependence of dynamic viscosity on shear rate and time-dependent viscosity recovery of these gels, their corresponding carbon dispersions containing 20 wt.% of carbon black (CB) and graphite (G) in a 25:75 ratio (CB.G/SG), and a reference carbon ink based on ethyl cellulose as an organic binder (CB.G/EC), are presented in Fig. 1.

The dependence of viscosity on the applied shear rate for the TiO_2-based gels is shown in Fig. 1a, where all samples exhibited shear-thinning behaviour, with viscosity decreasing as the shear rate increased due to the disruption of intermolecular interactions. A rapid decrease in viscosity up to a shear rate of 5 s^{-1} was observed for gels containing 0.5–1.5 wt.% PVP (SG0.5–SG1.5). In contrast, gels with higher PVP content (≥ 2 wt.%, SG2–SG3) showed a more pronounced viscoelastic character, reflected by a less significant decrease in viscosity and a shift of the minimum viscosity towards higher shear rates (~ 15 s^{-1}). The effect of PVP content was also reflected in the measured viscosity values, which increased remarkably from 1057 Pa.s for SG0.5 (0.5 wt.% PVP) to 6691 Pa.s for SG3 (3 wt.% PVP) at a shear rate of 0.1 s^{-1}. A comparable trend was observed at high shear rates (100 s^{-1}), where the minimum values ranged from 1.5 to 12.9 Pa.s, as summarized in Table 2. The high initial viscosity and its substantial decrease to low values can be attributed to the three-dimensional structure of the TiO_2 gels, formed by an interconnected network of TiO_2 nanoparticles. This structure is relatively weak and easily deforms under applied shear, leading to the disruption of particle–particle interactions and the breakdown of the network[47]. The addition of PVP increases the number of intermolecular interactions within the system, which contributes to the observed increase in viscosity with higher polymer content[48].

The rheological behaviour of the screen-printing carbon/TiO_2 inks prepared using the TiO_2-based binders (CB.G/SG) is shown in Fig. 1c. Like the pure TiO_2 inorganic binders, all inks exhibited shear-thinning behaviour. In contrast to the reference carbon ink based on the organic binder ethyl cellulose (CB.G/EC), the viscosity of CB.G/SG dispersions decreased rapidly at low shear rate (~ 20 s^{-1}). The CB.G/EC exhibited a more gradual viscosity reduction over the entire shear rate range (Fig. 1b), which is generally

preferred for screen-printing because it enables more controlled flow of the ink during printing[49,50]. The lower viscosity value of the CB.G/EC reference ink (7 Pa.s at 0.1 s^{-1}) is caused by the presence of non-crosslinked, linear ethyl cellulose chains dissolved in the solvent, where only weak physical entanglements and polymer–solvent interactions contribute to flow resistance. In contrast, sol–gel systems undergo hydrolysis and condensation reactions, leading to the formation of a progressively interconnected inorganic network that significantly restricts molecular mobility and increases viscosity. Consequently, the absence of a rigid three-dimensional network in the ethyl cellulose-based ink results in a substantially lower viscosity than in sol–gel-derived systems[51]. From the viscosity point of view, incorporating carbon black and graphite particles into TiO_2 gels, resulting in CB.G/SG inks, led to a higher viscosity compared to the corresponding binders (Table 2). This is related to the increasing number of interactions among TiO_2 particles, polymer chains, and carbon particles, resulting in a more complex, interconnected microstructure that exhibits higher resistance to flow at low shear rates (0.1 s^{-1})[52,53]. Under higher shear rate (100 s^{-1}), the viscosity decreases to values suitable for screen-printing technology, indicating the potential applicability of these carbon/TiO_2 inks[54,55].

Evaluation of time-dependent rheological behaviour is essential for screen-printing technology, where the ink must exhibit rapid structural recovery after shear-induced breakdown to preserve pattern definition and dimensional stability[53]. The thixotropic behaviour of the TiO_2-based binders (SG0.5–SG3), corresponding carbon dispersions (CB.G/SG) and reference carbon-based ink (CB.G/EC) was investigated using a three-interval thixotropy test (3ITT), consisting of an initial low shear rate (0.1 s^{-1} for 180 s), followed by a high shear rate (100 s^{-1} for 30 s) to simulate deformation through the mesh by the squeegee, and a final low shear interval (0.1 s^{-1} for 600 s) to monitor viscosity recovery, which is crucial for the levelling stage required to achieve uniform film formation. The viscosity recovery was evaluated as the percentage ratio of the viscosity values measured at a shear rate of 0.1 s^{-1} in the first and the third interval of the 3ITT. The time-dependent rheological behaviour of the TiO_2-based gels with varying PVP content is presented in Fig. 1d. All samples exhibited typical thixotropic behaviour, characterized by a pronounced drop in viscosity with applied shear rate of 100 s^{-1} confirming structural breakdown of the gel network, followed by a gradual increase in viscosity during the third interval at low shear rate (0.1 s^{-1}), indicating progressive regeneration of the internal structure[56–58]. The highest viscosity recovery (100 %) obsrved for the TiO_2 gel with the lowest PVP content (0.5 wt.%, SG0.5) can be attributed to its relatively low initial viscosity compared to the other TiO_2 gels with higher PVP content and its less interconnected structure, which allows rapid reconstruction of the internal network. With increasing PVP content, the initial viscosity increases, while the viscosity recovery decreases to 46 % for G3, and the time required to reach a steady state is prolonged. This behaviour is consistent with previous studies on polymer-containing gel systems, in which network reconstruction after shear is governed by the slow reformation of intermolecular and interparticle interactions. In systems with higher polymer content, the formation of a more densely interconnected structure further limits the mobility of structural units, resulting in slower relaxation dynamics and reduced recovery[58,59].

The time-dependent rheological behaviour of the carbon dispersions based on TiO_2 inorganic binders (CB.G/SG) is shown in Fig. 1f, where all inks exhibited thixotropic behaviour. The incorporation of CB and G particles into the TiO_2 gels resulted in a longer time required to reach a constant viscosity level, indicating slower structural recovery compared to the pure inorganic binders and suggesting a more prolonged levelling stage after screen-printing. On the other hand, the reference ink CB.G/EC reached the constant viscosity immediately after the applied shear, with viscosity recovery of 73% (Fig. 1e). Similarly to the inorganic binders, an increase in PVP content led to a subsequent decrease in viscosity recovery, as summarized in Table 2. The carbon inks containing TiO_2 binders with lower PVP content (CB.G/SG0.5–CB.G/SG1.5) exhibited higher recovery values (89–75%) compared to the reference ink. However, with a further increase in PVP content, the recovery decreased to 49% for CB.G/SG3, indicating slower structural rebuilding in systems with higher polymer content.

Table 2

Dynamic viscosity values at 0.1 and 100 s^{-1} and viscosity recovery for TiO_2-based binders and their corresponding carbon inks in comparison with the reference ink.

TiO_2 inorganic binder	**Dynamic viscosity (Pa.s) at 0.1 s^{-1}/100 s^{-1}**	**Viscosity recovery (%)**	**Carbon inks (CB.G)**	**Dynamic viscosity (Pa.s) at 0.1 s^{-1}/100 s^{-1}**	**Viscosity recovery (%)**
			CB.G/EC (Ref.)	**7.0/3.1**	**73**
SG0.5	1057/1.5	100	CB.G/SG0.5	3674/10.8	89
SG1	1884/3.9	83	CB.G/SG1	4250/12.7	79
SG1.5	2368/6.1	79	CB.G/SG1.5	4952/12.7	75
SG2	3699/9.0	73	CB.G/SG2	5540/14.9	72
SG2.5	5957/11.2	47	CB.G/SG2.5	6139/15.5	66
SG3	6691/12.9	46	CB.G/SG3	6906/17.2	49

Printability of carbon/TiO_2 inks was further evaluated by preparing screen-printed fine lines with widths of 0.15–0.50 mm onto a glass substrate. The widths of the printed structures were determined by optical microscopy and compared with the stencil dimensions. The results are shown in Fig. 2a, where the legend represents the stencil line width and the data points correspond to the measured widths of the printed structures for CB.G/SG inks and the reference ink (CB.G/EC). In the case of reference carbon ink (CB.G/EC), the printed structures exhibited pronounced line spreading with noticeable deviation from the stencil-defined dimensions. The maximum printable resolution was limited to a 0.35 mm line pattern, while the average real width of the printed lines was 0.65 mm. This originates from the lower viscosity of the reference ink, leading to deformation of the printed pattern and ultimately resulting in the formation of a continuous layer. As shown in Fig. 2b, a line defined by a stencil width of 0.40 mm had an actual

width of 0.74 ± 0.04 mm. Relative to the CB.G/EC reference, carbon/TiO_2 inks showed reduced line width across all investigated pattern dimensions with increasing PVP content in inorganic binders (Fig. 2a), and no merging of the adjacent lines was observed. However, inks with lower PVP content of 0.5–1.5 wt.% (CB.G/SG0.5–CB.G/SG1.5) exhibited limited reproduction accuracy with respect to the designed geometry. The highest resolved structures (0.25 mm stencil width) corresponded to average printed line widths ranging from 0.34 mm for CB.G/SG0.5 to 0.29 mm for CB.G/SG1.5. The poor edge definition and insufficient dimension stability shown in Fig. 2c are affected by lower ink viscosity under the applied shear of the squeegee, followed by rapid and high viscosity recovery after printing. In contrast, higher PVP content (2–3 wt.%) in CB.G/SG2–CB.G/SG3 inks increases resistance to flow during printing, resulting in improved shape retention of the printed structures on the glass substrate despite lower viscosity recovery. Consequently, print quality improved, as evidenced by narrower lines, well-defined edges (Fig. 2d), and the ability to fabricate high-resolution features with 0.20 mm line widths (Fig. 2e). The highest dimensional accuracy with respect to the stencil-defined pattern was obtained for the CB.G/SG3 ink, with the printed lines of 0.22 ± 0.02 mm. Although line patterns with a stencil width of 0.15 mm could also be printed, their continuity was limited by the screen-printing mesh.

(b) CB.G/EC, (c) CB.G/SG0.5, and (d) CB.G/SG3. (e) The highest resolution of 0.20 mm achieved for CB.G/SG3

Properties of carbon/TiO screen-printed electrodes

The effect of TiO_2 inorganic binder composition on the chemical structure of the sintered screen-printed carbon/TiO_2 composite electrodes, as well as the presence of the individual components, was investigated using Raman spectroscopy. To clarify the effect of the carbon phase on the characteristics of the TiO_2 particles, pristine sintered layers of employed inorganic binders were also prepared (Fig. 3a). Spectra of TiO_2 are characterized by intense vibrational mode E_g at 142 cm^{-1} as an indicator for the presence of anatase crystal structure, while other bands of anatase B_{1g}, A_{1g} and E_g are also observed at 394 cm^{-1}, 514 cm^{-1} and 636 cm^{-1}, which were consistent for all TiO_2 samples, regardless of the PVP content in the TiO_2 binders[60–62]. Additionally, the approximate crystallite size of TiO_2 (~ 20 nm) was estimated from the full widths of half maximum (FWHMs) of the most intense E_g mode (12.8 ± 0.2 cm^{-1})[46]. Since the band positions and FWHM did not change significantly, the anatase crystal structure and approximate crystallite size can be considered essentially unchanged. The slight increase in Raman intensity with increasing PVP content may therefore be associated with a higher amount of continuously distributed TiO_2 within the probed volume, resulting in more effective Raman scattering[62–64].

The Raman spectra of the composite carbon/TiO_2 electrodes (CB.G/SG) and the reference carbon electrode (CB.G/EC) were dominated by the characteristic D and G bands of the graphitic structure at 1350 cm^{-1} and 1590 cm^{-1} (Fig. 3b)[65]. The G band is a characteristic signature of graphitic carbon materials and corresponds to the stretching vibration of sp^2-hybridized carbon atoms within the carbon

lattice. The D band is associated with structural disorder in the graphitic network and arises from defects that activate the breathing vibrations of sp^2 carbon rings, including edge sites, vacancies, and functional groups[66–69]. For the composite CB.G/SG electrodes, the incorporation of TiO_2 into the carbon structure did not lead to any shifts of the D and G bands compared to the CB.G/EC reference, suggesting that the addition of TiO_2 did not introduce detectable structural modifications into the carbon phase under the applied processing conditions. Furthermore, the E_g vibrational mode at ~ 144 cm^{-1} was detected in all composite electrodes, confirming the presence of the anatase crystalline phase of TiO_2, and its position remained constant as PVP content in the inorganic binder increased. From the corresponding FWHM of E_g vibrational band (12.7–15.0 cm^{-1}), the TiO_2 crystallite size was estimated in the range of 11–17 nm, which also correlates with literature focused on sol–gel-derived carbon/TiO_2 systems, where the presence of a carbon phase was found to limit TiO_2 crystallite growth[70–72]. Regarding the Raman spectra of the EC and PVP polymers, no attributable bands were identified in either the reference electrode or the composite carbon/TiO_2 electrodes, which is consistent with their complete degradation during the sintering process.

The morphology and microstructure of the screen-printed carbon/TiO_2 composite electrodes and sintered pristine TiO_2 layers prepared from the studied TiO_2 inorganic binders were observed by SEM/EDS. As shown in Fig. 4a, the TiO_2 layer prepared with 1 wt.% PVP (SG1) exhibits a relatively compact and continuous structure disrupted by cracks caused by thermal stress during the sintering process. At higher magnification (50 000 ×), nanoscale features on the surface of the larger agglomerates were observed, which have not yet developed into well-defined particles, showing a limited influence of the low PVP content on particle formation. In Fig. 4b, increasing the PVP content to 2 wt.% (SG2) and its subsequent thermal decomposition during sintering resulted in a gradual breakdown of large agglomerates (~ 30 µm) to smaller ones (~ 1 µm) with spherical structure. This represents a transitional stage between the initially compact, bulky structure and the development of clearly defined aggregates of TiO_2 nanoparticles at higher PVP concentrations. The observed microstructural changes arise from interactions between PVP and Ti precursor species during the sol–gel synthesis, combined with steric stabilization by the polymer chains, which promotes a more homogeneous distribution of TiO_2 and suppresses particle agglomeration during thermal treatment[38,73]. The most pronounced stabilizing effect is evident at the highest PVP content of 3 wt.% (Fig. 4c), where the microstructure of the sintered layer (SG3) consists of TiO_2 nanoparticle clusters with sizes ranging from several hundred nanometres up to approximately 1 µm. The uniform spherical shape of the aggregates and their homogeneous distribution on the substrate correlate with the higher Raman band intensities observed in the SG3 sample.

In contrast to the pure TiO_2 layers, the addition of TiO_2 to the carbon structure of the CB.G/SG composite electrodes led to the formation of a continuous TiO_2 matrix connecting carbon particles and acting as a binder, rather than forming discrete spherical nanoparticle clusters. The screen-printed reference electrode (CB.G/EC) exhibits a porous structure formed by graphite flakes with a layered morphology

with particle sizes on the order of units to tens of μm, and spherical carbon black nanoparticles (20–50 nm) homogeneously distributed over their surface and connecting surrounding graphite particles (Fig. 4d). The surface microstructure of the composite carbon/TiO_2 electrode CB.G/SG1, based on a TiO_2 inorganic binder with a PVP content of 1 wt.%, is characterized by thin TiO_2 coating on carbon particles with pronounced cracks, while the fine interparticle connections of carbon black and TiO_2 were observed between the graphite flakes at higher magnification (Fig. 4e). Increasing PVP content results in a thicker TiO_2 coating and a more continuous structure covering carbon particles, accompanied by reduced crack density and effective filling of voids between carbon black and graphite, as demonstrated in Fig. 4f. The higher degree of surface homogeneity was achieved for CB.G/SG1.5–2.5 layers, corresponding to PVP contents of 1.5–2.5 wt.%. Meanwhile, a further increase in PVP content to 3 wt.% was accompanied by a renewed increase in crack density in the composite electrode CB.G/SG3.

The TiO_2 nanoparticles could not be directly determined from SEM images, but their size is assumed to be comparable to that of carbon black nanoparticles, based on Raman spectroscopy results. Therefore, information about the presence and distribution of TiO_2 was primarily obtained from EDS elemental analysis (Fig. 5). The reference electrode (CB.G/EC) exhibits a relatively high density of defects in the form of exposed substrate regions, confirmed by the detection of Sn originating from the conductive FTO substrate. These defects are caused by degradation of the EC. On the other hand, EDS mapping images of the CB.G/SG1 and CB.G/SG2 composite electrodes show a uniform distribution of Ti, indicating effective homogenization during ink preparation, contributing to the successful incorporation of TiO_2 within the composite layer. At the same time, the presence of exposed substrate areas decreases as PVP content increases up to 2.5 wt.%.

and (f) CB.G/SG2 corresponding to carbon/TiO_2 composite electrodes.

Insets show 50 000 × magnification details.

The mechanical stability of the printed carbon/TiO_2 composite electrode layers to the FTO substrate was evaluated by an adhesive tape test under controlled conditions, followed by optical density measurement of the detached layer residues. A decrease in optical density, corresponding to a lower amount of detached layer fragments, expresses improved interparticle cohesion and adhesion of the printed layer to the FTO substrate[45]. For the reference electrode CB.G/EC consisting of carbon material without EC binder after sintering, the entire printed layer detached from the substrate, resulting in the highest optical density value (Fig. 6a). Regarding the varying PVP content in inorganic binders, a gradual decrease in optical density was observed from CB.G/SG0.5 to CB.G/SG2.5 reflecting stronger adhesion of the printed layer to the substrate with increasing PVP content up to 2.5 wt.%. This trend is consistent with the SEM/EDS findings, which showed that PVP promotes the formation of a more uniform TiO_2 network interconnecting the carbon particles. In contrast, the reduced adhesion of the CB.G/SG3 electrode with the highest PVP content (3 wt.%) may arise from structural defects formed during sintering, making the layer more susceptible to detachment during the adhesive tape test.

Along with the enhanced mechanical stability of the printed composite CB.G/SG electrodes, a continuous increase in sheet resistance (R_{sh}) was recorded with increasing PVP content in the inorganic binder (Fig. 6b). Nevertheless, the sheet resistance remained significantly lower for all CB.G/SG electrodes than for the reference CB.G/EC electrode (R_{sh} = 327 Ω/sq), with the lowest values obtained for CB.G/SG0.5 (R_{sh} = 73 Ω/sq) and CB.G/SG1 (R_{sh} = 79 Ω/sq). The overall decrease in sheet resistance after incorporation of the TiO_2-based inorganic binder can additionally be explained by SEM observations, which suggest that at lower PVP contents, the TiO_2 nanoparticles formed only a partial coating on the graphite and carbon black particles, improving interparticle connectivity while preserving the conductive carbon network. A further increase in PVP content led to the formation of a thicker and more continuous network of semiconducting TiO_2 nanoparticles, which more extensively covered the conductive carbon structure and consequently increased the sheet resistance. Even so, the highest value measured for CB.G/SG3 electrode (R_{sh} = 172 Ω/sq) remained nearly two times lower than that of the CB.G/EC reference.

Properties of carbon/TiO_2 screen-printed counter electrodes in DSSC

To evaluate the electrochemical properties of screen-printed composite CB.G/SG counter electrodes (CEs) and standard platinum CE, cyclic voltammetry (CV) was carried out in an acetonitrile solution containing 1.10^{-3} M I_2, 1.10^{-2} M LiI, and 0.1 M $LiClO_4$. The CB.G/EC reference CE was excluded from the CV measurements due to its poor mechanical stability in the electrolyte, which caused disintegration of the carbon layer and electrolyte contamination. The cyclic voltammogram of the standard Pt CE exhibited two pairs of oxidation and reduction peaks at E_{ox1} = 0.36 V, E_{ox2} = 0.75 V, E_{red2} = 0.55 V, and E_{red1} = – 0.21 V, corresponding to the redox reactions of the I_3^-/I^- electrolyte, as described in Fig. 7a. Since the primary role of the CE in DSSCs is to catalyse the reduction of triiodide (I_3^-) to iodide (I^-), the peak-to-peak separation (E_{pp}) between E_{ox1} and E_{red1} and the corresponding peak current densities (J_{ox1} and J_{red1}) were analysed (Table 3). A smaller E_{pp} and higher J_{red} values are generally associated with faster charge-transfer kinetics and higher catalytic activity of the CEs[74,75]. As shown in Fig. 7b, the composite carbon/TiO_2 CEs (CB.G/SG) exhibit cyclic voltammograms similar in shape to the Pt CE, with E_{pp} values close to Pt (0.59 V), indicating comparable overpotential corresponding to the catalytic reaction[76]. At the same time, all composite CB.G/SG CEs showed higher oxidation and reduction peak current densities than Pt (J_{ox} = 1.64 mA.cm^{-2}, J_{red} = 1.30 mA.cm^{-2}). The higher catalytic activity is associated with their porous carbon-based structure, which provides a larger electrochemically active surface area and more accessible active sites for the I_3^-/I^- redox reaction[77,78]. Within the composite CB.G/SG CEs, increasing the PVP content in the corresponding TiO_2-based inorganic binder up to 2.5 wt.% led to a slight gradual decrease in the reduction peak current density J_{red}, from 1.48 mA.cm^{-2} for CB.G/SG0.5 to 1.36 mA.cm^{-2} for CB.G/SG2.5. This decrease is likely related to more extensive TiO_2

coverage of carbon particles at higher PVP contents, which may reduce the accessible electrochemically active surface area. In contrast, the absence of a clear E_{pp} trend suggests that the overall charge-transfer kinetics was not markedly affected by the binder composition.

Electrochemical impedance spectroscopy (EIS) revealed only a modest effect of the TiO_2-based inorganic binder composition on the charge-transfer properties of the screen-printed carbon CEs (Fig. 7c, Table 3). The carbon electrode with organic binder ethyl cellulose (CB.G/EC) exhibited the highest charge transfer resistance (R_{ct} ~33 Ω.cm^2), indicating limited interfacial kinetics of the I_3^-/I^- redox couple. Although this electrode could not be evaluated by CV, it was successfully characterized by EIS due to mechanical stabilization in the symmetrical cell configuration. Incorporation of TiO_2 binders decreased R_{ct} to ~ 22–19.5 Ω.cm^2 for the CB.G/SG electrodes. The small variation among individual samples indicates that R_{ct} is only weakly influenced by the TiO_2 binder composition, while the main contribution of the binder is related to improved particle connectivity and adhesion to the FTO substrate. Nevertheless, all carbon-based CEs still exhibited higher R_{ct} than Pt (9.65 Ω.cm^2), confirming the superior intrinsic catalytic activity of platinum toward the I_3^- reduction reaction. The series resistance (Rs) remained within a narrow range of ~ 11–13 Ω.cm^2 for all TiO_2-containing electrodes, indicating that PVP addition did not significantly disrupt the macroscopic conductivity pathways within the electrode, but rather reflects a balance between improved interparticle contact and the presence of less-conductive TiO_2 domains.

Table 3
Electrochemical parameters of the investigated counter electrodes obtained from CV and EIS measurements.

CE sample	**J_{ox1} (mA.cm^{-2})**	**J_{red1} (mA.cm^{-2})**	**E_{pp} (V)**	**R_{ct} (Ω.cm^2)**	**R_s (Ω.cm^2)**
Pt ref.	1.64 ± 0.20	1.30 ± 0.17	0.59 ± 0.05	9.65 ± 0.75	9.92 ± 0.69
CB.G/EC	-	-	-	32.99 ± 0.55	13.20 ± 0.70
CB.G/SG0.5	1.88 ± 0.14	1.48 ± 0.07	0.63 ± 0.04	22.05 ± 0.63	11.12 ± 0.88
CB.G/SG1	1.92 ± 0.09	1.44 ± 0.14	0.59 ± 0.03	21.43 ± 0.67	12.06 ± 0.17
CB.G/SG1.5	1.99 ± 0.09	1.40 ± 0.02	0.62 ± 0.03	20.53 ± 1.20	12.55 ± 0.35
CB.G/SG2	2.04 ± 0.17	1.37 ± 0.10	0.60 ± 0.02	20.56 ± 1.18	13.06 ± 0.22
CB.G/SG2.5	2.04 ± 0.07	1.36 ± 0.09	0.60 ± 0.03	20.01 ± 1.08	12.60 ± 0.25
CB.G/SG3	1.90 ± 0.09	1.43 ± 0.04	0.61 ± 0.02	19.54 ± 0.52	13.08 ± 0.60

As evidenced by Table 4, under standard illumination (100 mW cm^{-2}, AM 1.5G) simulating solar irradiation, the DSSCs employing composite CB.G/SG CEs based on TiO_2 inorganic binders reached

PCEs of 5.67–6.22%, remaining below that of the standard DSSC with the Pt CE (PCE = 8.21%). This lower performance can be attributed to slower charge-transfer kinetics at the CE/electrolyte interface, as reflected by the higher R_{ct} values of the composite CEs relative to Pt. The highest efficiency within the CB.G/SG CEs was achieved for CB.G/SG2.5 (PCE = 6.22%). As suggested by the J–V curves in Fig. 8a and confirmed by the photovoltaic parameters in Table 4, this DSSC still did not reach the performance of the Pt CE, mainly due to its lower fill factor (FF) and higher series resistance (R_s). In comparison with the reference DSSC with ethyl cellulose-based CE (CB.G/EC), which reached an efficiency of 5.78%, the DSSCs employing CB.G/SG CEs exhibited slightly higher or comparable PCEs together with lower R_s, as the incorporation of the TiO_2 inorganic binder improved interparticle contact and charge transport within the carbon layer. Considering the variation of PVP content in TiO_2-based inorganic binders used for the CB.G/SG CEs, no clear trend in the photovoltaic parameters of the corresponding DSSCs was evident. The resulting DSSC performance, however, is not determined solely by the properties of the CE, but also by the quality of the photoanode, charge recombination at the photoanode/electrolyte interface, and the spacing and contact between the individual components of the cell[79].

Table 4
Photovoltaic parameters of DSSCs with carbon black/graphite/TiO_2 composite CEs (CB.G/SG), carbon black/graphite CE (CB.G/EC), and Pt CE

100 mW.cm^{-2}					
CE sample	J_{sc} (mA.cm^{-2})	U_{oc} (V)	FF (%)	R_s (Ω.cm^2)	PCE (%)
Pt	19.90 ± 0.58	0.750 ± 0.007	55.04 ± 2.36	11.90 ± 1.13	8.21 ± 0.50
CB.G/EC	18.97 ± 0.60	0.752 ± 0.003	40.51 ± 1.59	41.66 ± 2.63	5.78 ± 0.19
CB.G/SG0.5	18.93 ± 1.14	0.751 ± 0.003	43.05 ± 1.78	28.61 ± 0.80	6.11 ± 0.28
CB.G/SG1	18.87 ± 0.20	0.749 ± 0.006	43.11 ± 1.44	30.28 ± 0.17	6.09 ± 0.27
CB.G/SG1.5	19.22 ± 1.17	0.749 ± 0.005	41.41 ± 1.58	32.32 ± 0.57	5.96 ± 0.33
CB.G/SG2	18.77 ± 0.33	0.744 ± 0.008	40.58 ± 1.05	33.51 ± 1.24	5.67 ± 0.18
CB.G/SG2.5	18.68 ± 0.41	0.752 ± 0.009	44.26 ± 0.32	30.25 ± 2.02	6.22 ± 0.10
CB.G/SG3	19.18 ± 0.61	0.750 ± 0.003	40.94 ± 0.71	32.96 ± 0.91	5.89 ± 0.20
1000 lux, 313 μW.cm^{-2} (200 lux, 63 μW.cm^{-2})					
CE sample	J_{sc} (μA.cm^{-2})	U_{oc} (V)	FF (%)	R_s (Ω.cm^2)	PCE (%)
Pt	130.26 ± 0.62 (23.64 ± 0.61)	0.579 ± 0.007 (0.512 ± 0.010)	75.15 ± 0.15 (73.41 ± 0.13)	229.0 ± 18.0 (1359.4 ± 97.5)	18.11 ± 0.17 (14.34 ± 0.08)
CB.G/EC	132.03 ± 2.67 (24.11 ± 0.57)	0.596 ± 0.008 (0.524 ± 0.011)	74.89 ± 0.39 (73.86 ± 1.02)	287.2 ± 7.6 (1323.9 ± 61.5)	18.83 ± 0.23 (15.06 ± 0.25)
CB.G/SG0.5	131.78 ± 0.15 (24.28 ± 0.28)	0.598 ± 0.002 (0.526 ± 0.002)	75.03 ± 0.50 (73.74 ± 0.55)	257.5 ± 6.3 (1268.5 ± 49.4)	18.88 ± 0.03 (15.20 ± 0.24)
CB.G/SG1	128.81 ± 0.92 (24.89 ± 0.15)	0.592 ± 0.003 (0.525 ± 0.003)	75.28 ± 0.08 (73.47 ± 0.13)	275.5 ± 7.4 (1223.0 ± 31.5)	18.33 ± 0.21 (15.49 ± 0.17)
CB.G/SG1.5	128.40 ± 1.15 (23.43 ± 0.03)	0.586 ± 0.005 (0.511 ± 0.006)	75.26 ± 0.56 (74.49 ± 0.39)	285.0 ± 11.3 (1364.8 ± 36.3)	18.10 ± 0.12 (14.39 ± 0.24)

100 mW.cm^{-2}					
CB.G/SG2	129.08 ± 0.27 (23.46 ± 0.49)	0.588 ± 0.001 (0.512 ± 0.002)	75.31 ± 0.04 (74.47 ± 0.50)	284.3 ± 0.2 (1428.8 ± 17.4)	18.26 ± 0.03 (14.43 ± 0.35)
CB.G/SG2.5	132.48 ± 2.27 (24.95 ± 0.37)	0.595 ± 0.010 (0.517 ± 0.008)	75.18 ± 0.34 (74.09 ± 1.56)	267.3 ± 4.6 (1295.4 ± 59.3)	18.94 ± 0.08 (15.41 ± 0.15)
CB.G/SG3	126.74 ± 0.70 (23.96 ± 0.76)	0.580 ± 0.001 (0.508 ± 0.003)	75.39 ± 0.03 (75.22 ± 0.38)	288.8 ± 3.0 (1292.3 ± 49.6)	17.71 ± 0.13 (14.78 ± 0.54)

Under indoor illumination (1000 and 200 lux), the advantage of the Pt CE became much less pronounced because the photocurrent density generated by the DSSC was reduced by approximately two to three orders of magnitude compared with AM 1.5G illumination. Under these low-current conditions, diffusion limitations in the electrolyte become less significant, and the higher charge-transfer resistance of the carbon/TiO_2 CEs was no longer sufficient to noticeably affect the overall photovoltaic performance[80]. As a result, the DSSCs employing CB.G/SG CEs achieved efficiencies comparable to, or slightly exceeding, those of the Pt reference with PCE 18.11 %at 1000 lux and 14.34 %at 200 lux. The representative J–V curves in Fig. 8b further illustrate this behaviour for the composite CE, CB.G/SG2.5 with the highest reached PCE of 18.94 %at 1000 lux. At reduced light intensity of 200 lux, the same DSSC reached a PCE of 15.41 %and J_{sc} of 24.95 μA.cm^{-2}, while a slightly higher PCE of 15.49 %was recorded for CB.G/SG1.

For the CB.G/SG2.5 composition, where 2.5 wt.% of PVP was used as a stabilizing agent in the TiO_2 inorganic binder, a suitable compromise was achieved between mechanical stability of the CE, its sheet resistance (R_{sh} = 149 Ω/sq), interconnection of the carbon particles ensured by TiO_2, and preservation of the electrochemically active surface. The PCE values of the DSSC with the CB.G/SG2.5 CE under standard illumination and indoor light at 1000 lux are compared in Table 5 with selected studies published over the last five years, highlighting its position among recently reported carbon-based and composite CEs for DSSCs.

Table 5
Comparison of power conversion efficiency of DSSCs with carbon-based counter electrodes under standard illumination and indoor light (1000 lux) reported in this work and previous studies.

CE	Photoanode	Electrolyte	PCE (%) (100 $mW.cm^{-2}$)	PCE (%) (1000 lux)	Ref.
CB.G/SG2.5	TiO_2/N719	I_3^-/I^-	6.22	18.94	This Work
CB/G:TTIP	TiO_2/N719	I_3^-/I^-	5.74	-	32
Biochar/TTIP	TiO_2/N719	I_3^-/I^-	6.43	-	33
CoSbS/MWCNT	TiO_2/N719	I_3^-/I^-	6.0	-	81
MoO_3/MoS_2-rGO	TiO_2/N719	I_3^-/I^-	5.0	-	82
PEDOT:PSS/GNP	TiO_2/YD2-*o*-C8	$[Co(bpy)]^{3+/2+}$	10.40	29.7	83
PEDOT/CB	TiO_2/Y123	$[Cu(dmby)]^{2+/1+}$	9.83	25.17	22
CB.G	TiO_2/Y123	Ti3C2 Mxene-$[Cu(dmp)]^{2+/1+}$ PEO/PVDF-HFP (quasi solid)	5.63	14.2	84
Flexible-LIG	TiO_2/N719	$[Cu(tmby)]^{2+/1+}$	4.96	9.64	85
Graphene	TiO_2/MS5:XY1b	IN11	-	14.3	86
PEDOT/GO	TiO_2/N719	I_3^-/I^- (quasi solid)	-	19.7	87

Conclusion

This work demonstrates the use of PVP-assisted sol–gel-derived TiO_2 inorganic binders as an alternative to ethyl cellulose in screen-printable carbon dispersions for DSSC counter electrodes. PVP acted as a stabilizing agent for the TiO_2 network, while the corresponding dispersions based on carbon black and graphite exhibited shear-thinning behaviour, thixotropy, and suitable printability, particularly at PVP contents of 2 wt.% and higher. After sintering of screen-printed CEs, the anatase TiO_2 phase was confirmed with crystallite sizes of ~ 11–17 nm, while increasing PVP content promoted TiO_2-mediated interconnection of carbon particles, improved layer homogeneity, and enhanced mechanical properties

compared to the ethyl cellulose-based CB.G/EC reference electrode. Among the composite CEs, CB.G/SG2.5, prepared with a binder containing 2.5 wt.% of PVP, exhibited the best adhesion to the FTO substrate and the most homogeneous layer, while maintaining a suitable sheet resistance of 149 Ω/sq and favourable electrochemical properties in the I_3^-/I^- electrolyte, with J_{red} of 1.36 $mA.cm^{-2}$ and R_{ct} of 20.01 $Ω.cm^2$. Under indoor illumination, the DSSC employing this CE achieved the highest efficiencies of 18.94% at 1000 lux and 15.41% at 200 lux, exceeding the Pt reference efficiencies of 18.11% (1000 lux) and 14.34% (200 lux), respectively. The proposed approach therefore provides a simple and scalable route toward mechanically stable, printable, and low-cost carbon counter electrodes as promising alternatives to Pt for indoor DSSC applications.

Declarations

Competing interests

The authors declare no competing interests.

Funding

This work was supported by the European Union NextGenerationEU through the Recovery and Resilience Plan for Slovakia under the project No. 09I03-03-V05-00005 (internal grant No. 23-04-04-A: CARBTIOSOLCELL). The contribution of the Scientific Grant Agency of the Ministry of Education of the Slovak Republic through grant VEGA 2/0136/24 is also acknowledged.

Author Contribution

T.B. performed the experimental work, analysed the data, prepared the figures and wrote the original draft. M.H. contributed to methodology development, process optimization and data analysis. I.V. contributed to material characterization and data analysis. R.S. and A.L. contributed to methodology and discussion of the results. P.G. conceived the study, supervised the work, contributed to experimental measurements, data analysis and interpretation, and revised the manuscript. All authors reviewed and approved the final manuscript.

Acknowledgement

The authors thank the Laboratory of Material Analyses of the Slovak National Gallery for access to Raman spectroscopy instrumentation and assistance with measurements.

Data Availability

All data supporting the findings of this study are available within the paper.

References

1. Scharber, M. C. Efficiency of Emerging Photovoltaic Devices under Indoor Conditions. *Solar RRL* **8**, (2024).
2. Raïssi, M. et al. Efficient Large Area Semi-Transparent Dye-Sensitized Solar Cells (DSSCs) Printed with DMD400 Technology. *Adv Mater. Technol* **9**, (2024).
3. Kang, H. C. et al. Scalable Fabrication of RGB-Color, Semi-Transparent DSSC Modules Enabled by a Printable Compact TiO2 Blocking Layer. *Mater Today Energy* **53**, (2025).
4. Sasitharan, K. & Freitag, M. From Zombies to Smart Devices: The Evolution of Dye-Sensitized Solar Cells for IoT Applications. *ACS Applied Energy Materials* 8, 9891–9899 Preprint at (2025). https://doi.org/10.1021/acsaem.5c00624
5. Iswarya, S., Dharshini, A. & Mary Vithiya, S. B. & Augustine Arul Prasad, T. Evolving smart homes to exploring space, dye-sensitized solar cells (DSSC) as a sustainable energy model for the future world—A review. *Next Energy* 8, Preprint at (2025). https://doi.org/10.1016/j.nxener.2025.100328
6. Khairudin, A. R. M., Aziz, N. A. S., Rahman, M. Y. A. & Umar, A. A. Metal oxide and its modification as photoanode for dye-sensitized solar cell: a review. *Journal of Materials Science: Materials in Electronics* vol. 37 Preprint at (2026). https://doi.org/10.1007/s10854-026-17282-0
7. Rahman, M. Y. A. Review of graphene and its modification as cathode for dye-sensitized solar cells. *Journal of Materials Science: Materials in Electronics* 32, 23690–23719 Preprint at (2021). https://doi.org/10.1007/s10854-021-06898-z
8. Njema, G. G., Elmelouky, A., Meyer, E. L., Riouchi, N. & Kibet, J. K. Pioneering an Innovative Eco-Friendly N719 Dye-Sensitized Solar Cell through Modelling and Impedance Spectroscopy Analysis for Energy Sustainability. *Global Challenges* **9**, (2025).
9. Kumar, S., Asif, M., Chand, M. & Sharma, S. Dye sensitized solar cell as eco friendly and low cost renewable energy solutions a mini review. *Discover Energy* **6**, (2026).
10. Prabakar, P., Mustafa Mert, K., Muruganandam, L. & Sivagami, K. A comprehensive review on biochar for electrochemical energy storage applications: an emerging sustainable technology. *Frontiers in Energy Research* 12, Preprint at (2024). https://doi.org/10.3389/fenrg.2024.1448520
11. Siddiqui, H. et al. Comprehensive review of carbon materials as counter electrodes in dye-sensitized solar cells: Efficiency assessment and deposition methods. *Materials Science in Semiconductor Processing* 172, Preprint at (2024). https://doi.org/10.1016/j.mssp.2023.108074
12. Samantaray, M. R. et al. Synergetic effects of hybrid carbon nanostructured counter electrodes for dye-sensitized solar cells: A review. *Materials* 13, 1–34 Preprint at (2020). https://doi.org/10.3390/ma13122779
13. Alizadeh, A. et al. Recent developments of perovskites oxides and spinel materials as platinum-free counter electrodes for dye-sensitized solar cells: A comprehensive review. *Renewable and*

Sustainable Energy Reviews 187, Preprint at (2023). https://doi.org/10.1016/j.rser.2023.113770

14. Don, M. F. et al. Acetylene carbon black-graphite composite as low-cost and efficient counter electrode for dye-sensitized solar cells (DSSCs). *Ionics (Kiel).* 25, 5585–5593 (2019).
15. Murugadoss, G. et al. Cost-effective carbon black-graphite composite with solid-state based CuSCN electrode for dye-sensitized solar cells. *Fuel* **348**, (2023).
16. Santos, F., Ivanou, D. & Mendes, A. Solvent-Dependent Charge Transfer Dynamics under Indoor Light in Efficient and Stable Copper-Mediated DSSCs. *ACS Appl. Energy Mater.* https://doi.org/10.1021/acsaem.6c01356 (2026).
17. Khazraei, S., Mikladal, B. F., Etula, J., Varjos, I. & Hannu, J. Dry deposited single-walled carbon nanotubes co-assisted with copper redox mediator-based electrolytes for photo-stability of dye-sensitized solar cells. *Electrochim Acta* **488**, (2024).
18. Hashmi, S. G., Sonai, G. G., Iftikhar, H., Lund, P. D. & Nogueira, A. F. Printed single-walled carbon-nanotubes-based counter electrodes for dye-sensitized solar cells with copper-based redox mediators. *Semicond Sci. Technol* **34**, (2019).
19. Tenywa, S., Inyalot, J. T. & Okello, A. Metal oxides and carbonaceous nanocomposites as platinum-free counter electrodes for dye sensitized solar cells; A review. *Heliyon* 11, Preprint at (2025). https://doi.org/10.1016/j.heliyon.2025.e43547
20. Meyer, E., Bede, A., Zingwe, N. & Taziwa, R. Metal sulphides and their carbon supported composites as platinum-free counter electrodes in dye-sensitized solar cells: A review. *Materials* 12, Preprint at (2019). https://doi.org/10.3390/ma12121980
21. Kanjana, N. et al. Biomass-derived rGO-like carbon from oil palm petioles integrated with NiO/PEDOT:PSS composites for counter electrodes in dye-sensitized solar cells. *Results Engineering* **29**, (2026).
22. Venkatesan, S., Chuang, I. T., Teng, H. & Lee, Y. L. High-Performance Carbon Black-Based Counter Electrodes for Copper (I)/(II)-Mediated Dye-Sensitized Solar Cells. *ACS Sustain. Chem. Eng.* **11**, 12166–12176 (2023).
23. Dissanayake, M. A. K. L. et al. A low-cost, vein graphite/tin oxide nanoparticles based composite counter electrode for efficient dye-sensitized solar cells. *Materials Sci. Engineering: B* **273**, (2021).
24. Don, M. F., Ekanayake, P., Nakajima, H., Mahadi, A. H. & Lim, C. M. Improvement of dye-sensitized solar cell performance through introducing TiO2 in acetylene carbon black-graphite composite electrode. *Thin Solid Films* **706**, (2020).
25. Zhang, S. et al. Increased power conversion efficiency of dye-sensitized solar cells with counter electrodes based on carbon materials. *RSC Adv.* **9**, 22092–22100 (2019).
26. Ahmed, A. S. A., Xiang, W., Hashem, F. S. M. & Zhao, X. Screen-printed carbon black/SiO2 composite counter electrodes for dye-sensitized solar cells. *Sol. Energy*. **230**, 902–911 (2021).
27. Rubio, J. C. & Bolduc, M. Screen Printing for Energy Storage and Functional Electronics: A Review. *Electronic Materials* 6, Preprint at (2025). https://doi.org/10.3390/electronicmat6020007

28. Islam, N. et al. Multifunctional Screen-Printed Conductive Inks: Design Principles, Performance Challenges, and Application Horizons. *ACS Applied Electronic Materials* 7, 7503–7544 Preprint at (2025). https://doi.org/10.1021/acsaelm.5c01256
29. Hatala, M. et al. Screen-printed conductive carbon layers for dye-sensitized solar cells and electrochemical detection of dopamine. *Chem. Pap.* **75**, 3817–3829 (2021).
30. Chang, C. et al. Review of the sol-gel method in preparing nano TiO2for advanced oxidation process. *Nanotechnology Reviews* 12, Preprint at (2023). https://doi.org/10.1515/ntrev-2023-0150
31. Muthee, D. K. & Dejene, B. F. Impact of Synthesis pH on Nano-structural, Opto-electronic, and Photocatalytic Properties of TiO2 Nanoparticles. *J. Nanostruct.* **11**, 305–316 (2021).
32. Narudin, N., Ekanayake, P., Soon, Y. W., Nakajima, H. & Lim, C. M. Enhanced properties of low-cost carbon black-graphite counter electrode in DSSC by incorporating binders. *Sol. Energy*. **225**, 237–244 (2021).
33. Buchlová, T. et al. Screen-printed counter-electrodes based on biochar derived from wood-corn silage and titanium isopropoxide binder as a more efficient and renewable alternative to Pt-CE for dye-sensitized solar cells. *Mater Sci. Semicond. Process* **171**, (2024).
34. Simonsen, M. E. & Søgaard, E. G. Sol-gel reactions of titanium alkoxides and water: Influence of pH and alkoxy group on cluster formation and properties of the resulting products. *J. Solgel Sci. Technol.* **53**, 485–497 (2010).
35. Muthee, D. K. & Dejene, B. F. The effect of tetra isopropyl orthotitanate (TIP) concentration on structural, and luminescence properties of titanium dioxide nanoparticles prepared by sol-gel method. *Mater Sci. Semicond. Process* **106**, (2020).
36. Wiranwetchayan, O., Promnopas, S., Thongtem, T., Chaipanich, A. & Thongtem, S. Effect of alcohol solvents on TiO2 films prepared by sol–gel method. *Surf. Coat. Technol.* **326**, 310–315 (2017).
37. Mirmohammad Sadeghi, S., Vaezi, M., Kazemzadeh, A. & Jamjah, R. Morphology enhancement of TiO2/PVP composite nanofibers based on solution viscosity and processing parameters of electrospinning method. *J Appl. Polym. Sci* **135**, (2018).
38. Wiranwetchayan, O., Promnopat, S., Thongtem, T., Chaipanich, A. & Thongtem, S. Effect of polymeric precursors on the properties of TiO2 films prepared by sol-gel method. *Mater Chem. Phys* **240**, (2020).
39. Chakraborty, S., Sarkar, I., Behera, D. K., Pal, S. K. & Chakraborty, S. Experimental investigation on the effect of dispersant addition on thermal and rheological characteristics of TiO2 nanofluid. *Powder Technol.* **307**, 10–24 (2017).
40. Chávez-Pérez, A. G., Escorcia-García, J. & González, L. A. Reyes-Vallejo, O. Tunning the optoelectronic properties of Sm3+-doped mesoporous TiO2 thin films via PVP assisted sol-gel process for solar cells. *J. Solgel Sci. Technol.* **113**, 985–1000 (2025).
41. Yadav, M., Singh, G. & Lata, S. Polyvinylpyrrolidone/TiO2 composites' preparation via sol–gel procedure furthered with non-enzymatic glucose sensing and antibacterial effectiveness. *Environ. Sci. Pollut. Res.* **30**, 98563–98580 (2023).

42. Pei, C., Zhu, J. H. & Lv, L. Enhanced visible-light induced photocatalytic activity in core-shell structured graphene/titanium dioxide nanofiber mats. *J Environ. Chem. Eng* **12**, (2024).
43. Nguyen, C. H., Lai, T. Q. & Tran, T. T. V. Immobilization TiO2 nanoparticles into alginate/PVP hydrogel beads for photocatalyst: effective antibiotic removal, superior recovery and reuse ability. *Int. J. Environ. Sci. Technol.* **22**, 6451–6466 (2025).
44. Khalafi, M., Nikfarjam, A., Hajghassem, H. & Bidmeshkipour, S. UV activated single aligned TiO2 nanofiber embedded silver nanoparticles as room temperature ammonia gas sensor. *Phys Scr* **98**, (2023).
45. Hatala, M., Gemeiner, P., Hvojnik, M. & Mikula, M. The effect of the ink composition on the performance of carbon-based conductive screen printing inks. *J. Mater. Sci.: Mater. Electron.* **30**, 1034–1044 (2019).
46. Fresno, F. et al. Influence of Sn4 + on the structural and electronic properties of Ti1-xSnxO2 nanoparticles used as photocatalysts. *Phys. Chem. Chem. Phys.* **8**, 2421–2430 (2006).
47. Saraswat, M. & Sengwa, R. J. Effects of PVP surfactant on nanosuspension stability and optical, dielectric, and rheological properties of zinc oxide nanoparticles dispersed alcohols mixture based nanofluids. *J Mol. Liq* **385**, (2023).
48. Ming, H. et al. Rheological behavior of particle-filled polymer suspensions and its influence on surface structure of the coated electrodes. *E-Polymers* **24**, (2024).
49. Mesa, S., Ramírez, E., Rivera Botia, K. G., Jaramillo, F. & Ramírez, D. Development and characterization of carbon-based conductive pastes with high mechanical integrity under bending stress for room-temperature printable electronics. *Sci Rep* **15**, (2025).
50. Tang, X. et al. Screen Printing of Silver and Carbon Nanotube Composite Inks for Flexible and Reliable Organic Integrated Devices. *ACS Appl. Nano Mater.* **5**, 4801–4811 (2022).
51. Pierre, A. C. *Introduction to Sol-Gel Processing* Vol. 1 (Springer New York, NY, 1998).
52. Potts, S. J. et al. The influence of carbon morphologies and concentrations on the rheology and electrical performance of screen-printed carbon pastes. *J. Mater. Sci.* **57**, 2650–2666 (2022).
53. Li, H., Liu, S., Li, X., Wu, Z. S. & Liang, J. Screen-printing fabrication of high volumetric energy density micro-supercapacitors based on high-resolution thixotropic-ternary hybrid interdigital micro-electrodes. *Mater. Chem. Front.* **3**, 626–635 (2019).
54. Liu, L., Shen, Z., Zhang, X. & Ma, H. Highly conductive graphene/carbon black screen printing inks for flexible electronics. *J. Colloid Interface Sci.* **582**, 12–21 (2021).
55. Go, M., Qi, X., Matteini, P., Hwang, B. & Lim, S. High resolution screen-printing of carbon black/carbon nanotube composite for stretchable and wearable strain sensor with controllable sensitivity. *Sens Actuators Phys* **332**, (2021).
56. Hasunuma, Y. et al. Morphology and Properties of Gel-Coating Films Containing Organo-Modified Inorganic Nanoparticles Exhibiting the Scattering Ability of Ultraviolet Radiation. *ChemistrySelect* 10, (2025).

57. Ge, J., Wu, Q., Ding, L., Guo, H. & Zhao, A. Preparation and rheological Evaluation of a thixotropic polymer gel for water shutoff in fractured tight reservoirs. *J Pet. Sci. Eng* **208**, (2022).
58. Grosskopf, A. K., Saouaf, O. A., Lopez Hernandez, H. & Appel, E. A. Gelation and yielding behavior of polymer–nanoparticle hydrogels. *J. Polym. Sci.* **59**, 2854–2866 (2021).
59. Wang, W., Hu, Y., Li, L., Zeng, J. & Yao, Y. Effect of various polymer additives on the rheology and thixotropy of organic vehicles. *J. Mater. Sci.: Mater. Electron.* **33**, 12002–12015 (2022).
60. Kéri, O. et al. Thermal properties of electrospun polyvinylpyrrolidone/titanium tetraisopropoxide composite nanofibers. *J. Therm. Anal. Calorim.* **137**, 1249–1254 (2019).
61. El-Deen, S. S. et al. Anatase TiO2 nanoparticles for lithium-ion batteries. *Ionics (Kiel)*. **24**, 2925–2934 (2018).
62. Rajkumar, D., Umamahesvari, H. & Nagaraju, P. Synthesis and characterization of anatase phase TiO2 thin films for formaldehyde detection. *Journal Mater. Science: Mater. Electronics* **35**, (2024).
63. Van Velson, N., Zobeiri, H. & Wang, X. Thickness-Dependent Raman Scattering from Thin-Film Systems. *J. Phys. Chem. C*. **127**, 2995–3004 (2023).
64. Igamov, B. D. et al. Comprehensive analysis of thickness-dependent structural, morphological, and optical properties of TiO2 based thin films. *Results Optics* **23**, (2026).
65. Poupart, R. et al. Carbon black structural effect within kraft black liquor-based poly(HIPE): enhanced hydrogen storage and electro-capacitive properties. *J. Mater. Chem. Mater.* **12**, 22703–22714 (2024).
66. Yuan, R. et al. Raman spectroscopy analysis of disordered and amorphous carbon materials: A review of empirical correlations. *Carbon* 238, Preprint at (2025). https://doi.org/10.1016/j.carbon.2025.120214
67. Cançado, L. G. et al. Science and Metrology of defects in graphene using Raman Spectroscopy. *Carbon* 220, Preprint at (2024). https://doi.org/10.1016/j.carbon.2024.118801
68. Mazzaracchio, V. et al. Inside the different types of carbon black as nanomodifiers for screen-printed electrodes. *Electrochim. Acta*. **317**, 673–683 (2019).
69. Dziejarski, B. et al. Chemical conversion of recovered carbon black (rCB) from end-of-life tires (ELTs) pyrolysis to reduced graphene oxide (rGO): From waste to advanced materials. *J. Mater. Chem. C Mater.* **13**, 2753–2767 (2024).
70. Shao, X., Lu, W., Zhang, R. & Pan, F. Enhanced photocatalytic activity of TiO 2 -C hybrid aerogels for methylene blue degradation. *Sci Rep* **3**, (2013).
71. Wang, M., Jin, C., Luo, Q. & Kim, E. J. Sol-gel derived TiO2–carbon composites with adsorption-enhanced photocatalytic activity and gas sensing performance. *Ceram. Int.* **46**, 18608–18613 (2020).
72. Tan, L. L., Ong, W. J., Chai, S. P. & Mohamed, A. R. Reduced graphene oxide-TiO2 nanocomposite as a promising visible-light-active photocatalyst for the conversion of carbon dioxide. *Nanoscale Res. Lett* **8**, (2013).

73. Vasudevan, P., Thomas, S., Biju, P. R., Sudarsanakumar, C. & Unnikrishnan, N. V. Synthesis and structural characterization of sol-gel derived titania/poly (vinyl pyrrolidone) nanocomposites. *J. Solgel Sci. Technol.* **62**, 41–46 (2012).
74. Kanjana, N. et al. & Amornkitbamrung, V. Fly ash boosted electrocatalytic properties of PEDOT:PSS counter electrodes for the triiodide reduction in dye-sensitized solar cells. *Sci Rep* **13**, (2023).
75. Gnanasekar, S., Kollu, P., Jeong, S. K. & Grace, A. N. Pt-free, low-cost and efficient counter electrode with carbon wrapped VO 2 (M) nanofiber for dye-sensitized solar cells. *Sci Rep* **9**, (2019).
76. Zhang, X., Wang, T., Li, X., Wu, D. & Chen, W. Nitrogen-doped carbon encapsulating γ-MoC/Ni nanoparticles as efficient counter electrodes for dye-sensitized solar cells. *J. Coord. Chem.* **73**, 2621–2631 (2020).
77. Liu, J. et al. Anchoring CoS on three-dimensional porous rGO thin films as efficient counter electrodes for dye-sensitized solar cells. *J. Mater. Sci.: Mater. Electron.* **31**, 22546–22553 (2020).
78. Wu, M. S. & Lin, J. C. Dual doping of mesoporous carbon pillars with oxygen and sulfur as counter electrodes for iodide/triiodide redox mediated dye-sensitized solar cells. *Appl. Surf. Sci.* **471**, 455–461 (2019).
79. Chandra Sil, M. et al. Enhancement of power conversion efficiency of dye-sensitized solar cells for indoor applications by using a highly responsive organic dye and tailoring the thickness of photoactive layer. *J Power Sources* **479**, (2020).
80. Michaels, H., Benesperi, I. & Freitag, M. Challenges and prospects of ambient hybrid solar cell applications. *Chemical Science* vol. 12 5002–5015 Preprint at (2021). https://doi.org/10.1039/d0sc06477g
81. Peter, I. J., Vijaya, S., Anandan, S., Karazhanov, S. & Nithiananthi, P. M. W. C. N. T. Aided Cobalt Antimony Sulfide Electrocatalyst for Dye-Sensitized Solar Cells and Supercapacitors: Designing Integrated Photo-Powered Energy System. *J. Electrochem. Soc.* **169**, 056518 (2022).
82. Sivakumar, V., Dharmajan, N., Jayaram, A., Mani, N. & Santhana Krishnan, H. Enhanced catalytic performance of MoO3/MoS2-rGO counter electrode towards a Pt-free dye sensitized solar cell. *Solar Energy Mater. Solar Cells* **285**, (2025).
83. Hora, C. et al. PEDOT-graphene counter-electrode for solar and improved artificial light conversion in regular, bifacial and FTO-less cobalt mediated DSSCs. *Electrochim Acta* **412**, (2022).
84. Khazraei, S. et al. MXene-modified polymer interfaces for stable quasi-solid dye-sensitized solar cells. *Carbon N Y* **252**, (2026).
85. Speranza, R., Reina, M., Zaccagnini, P., Pedico, A. & Lamberti, A. Laser-induced graphene as a sustainable counter electrode for DSSC enabling flexible self-powered integrated harvesting and storage device for indoor application. *Electrochim Acta* **460**, (2023).
86. Salleh, S. A., Rahman, M. Y. A., Aziz, T. H. T., Sauvage, F. & Beddu, S. Influence of number of layer of graphene films as counter electrode for efficient dye-sensitized solar cell in indoor application. *Chem. Pap.* **79**, 723–731 (2025).

87. Vajda, M. et al. Poly (3, 4-ethylenedioxythiophene) (PEDOT) decorated with graphene oxide as sustainable Pt-free counter electrode for indoor dye-sensitized solar cells. *Surfaces Interfaces* **72**, (2025).

Figures

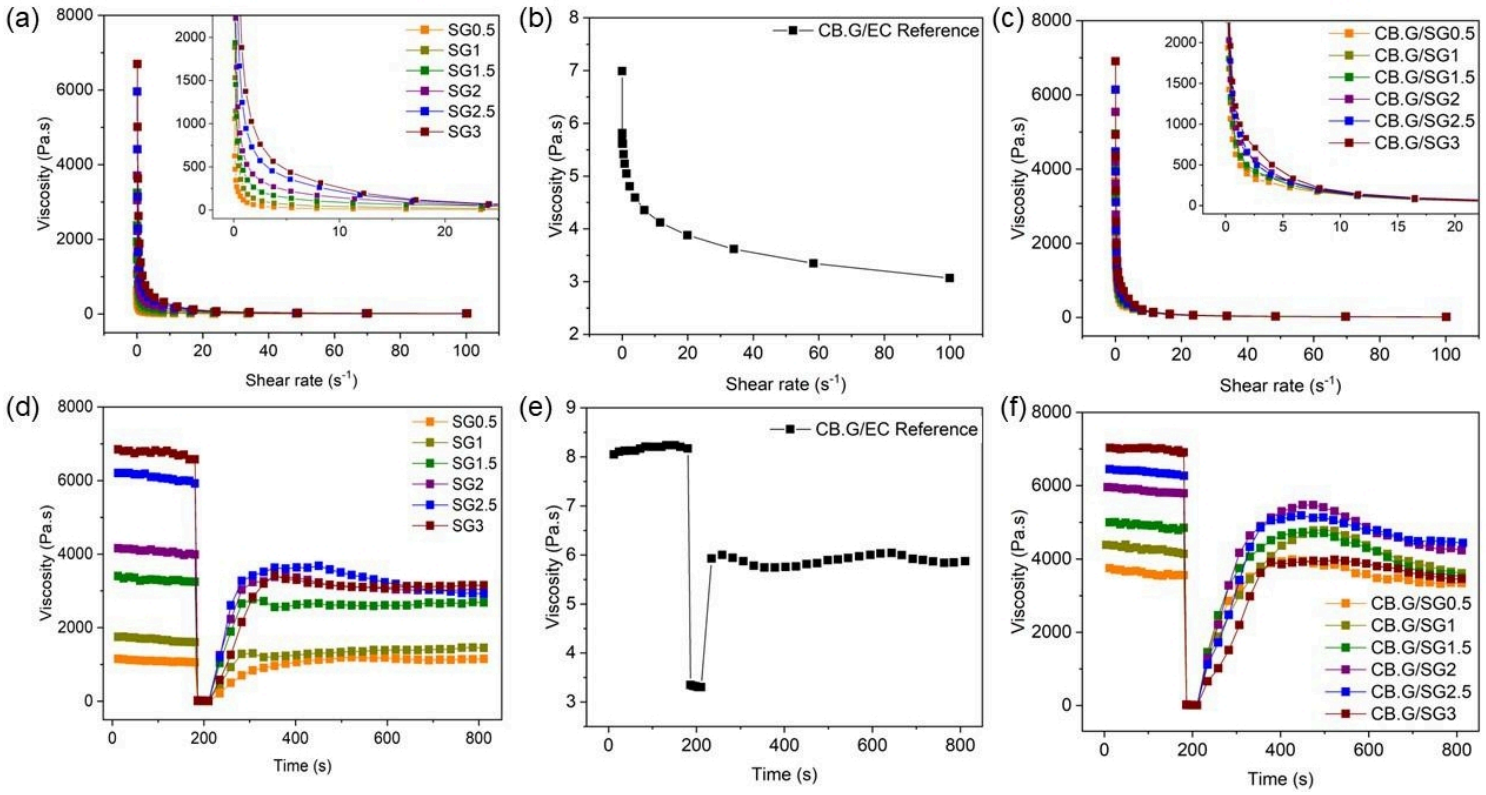


Figure 1

Viscosity as a function of shear rate for (a) TiO_2-based inorganic binders with varying PVP content, (b) reference ink with ethyl cellulose binder (CB.G/EC), and (c) carbon/TiO_2 inks (CB.G/SG). Time-dependent behaviour during the 3ITT for (d) TiO_2-based binders, (e) reference ink (CB.G/EC), and (f) carbon/TiO_2 inks.

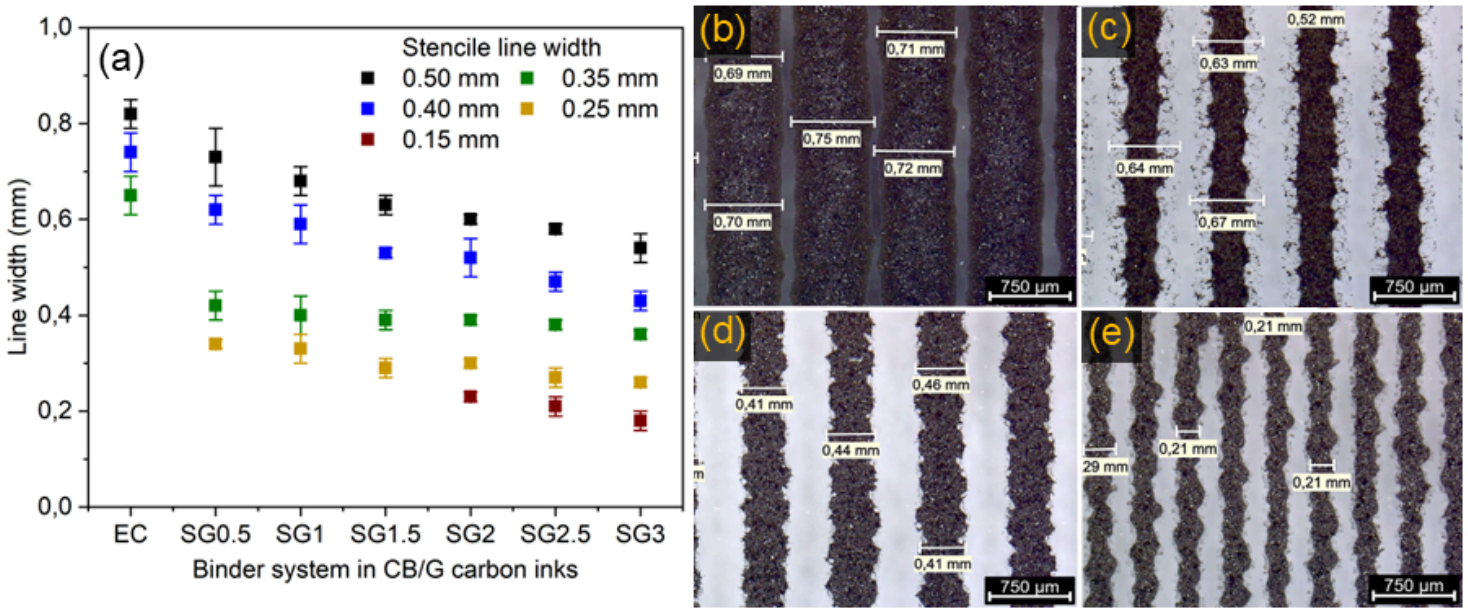


Figure 2

Printability of carbon inks: (a) Stencil-defined vs. measured line widths for CB.G/SG inks and the reference (CB.G/EC). Optical microscopy images (200 × magnification) of 0.40 mm lines for (b) CB.G/EC, (c) CB.G/SG0.5, and (d) CB.G/SG3. (e) The highest resolution of 0.20 mm achieved for CB.G/SG3

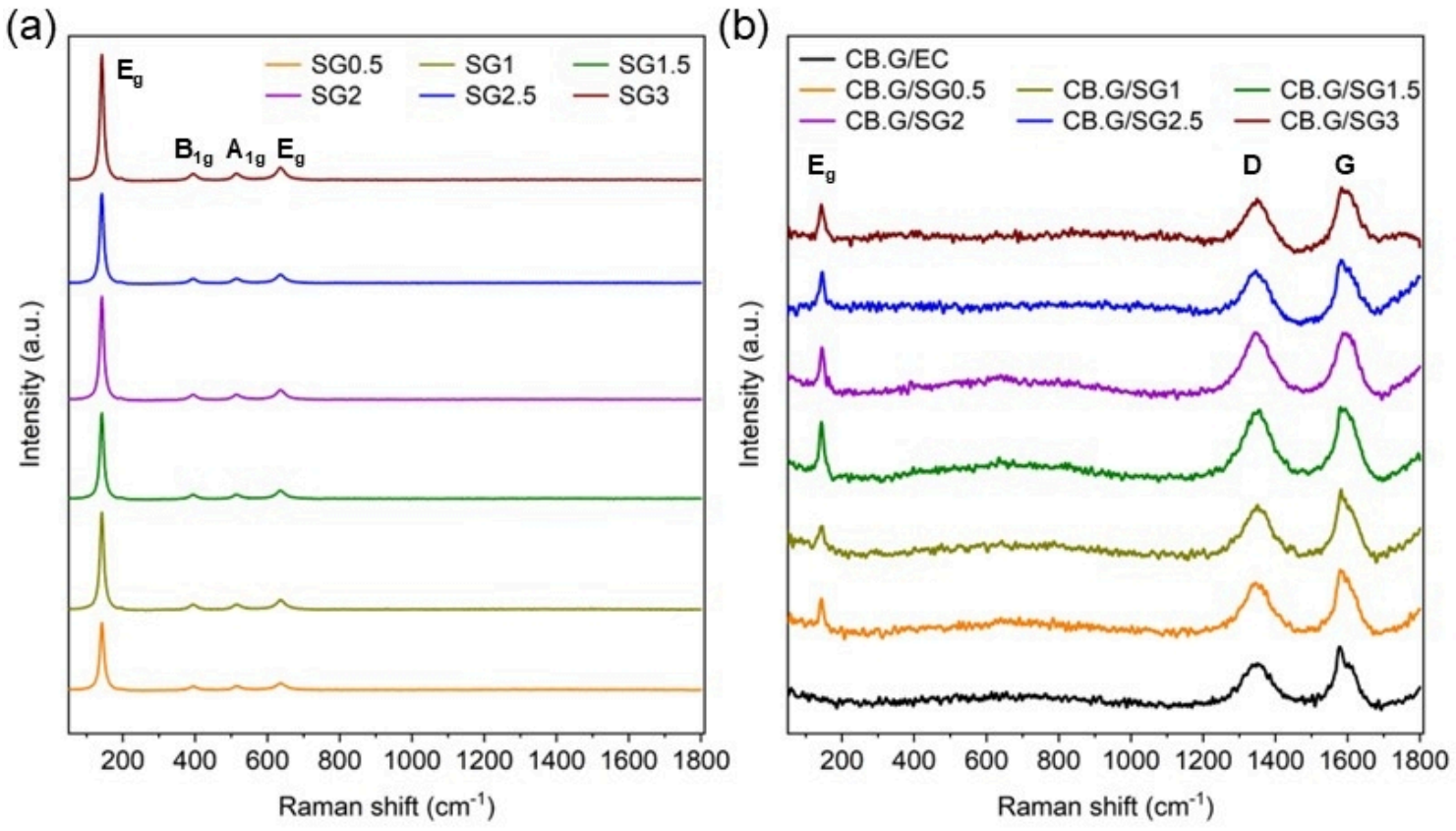


Figure 3

Raman spectra of (a) pristine TiO_2 layers from the investigated inorganic binders and (b) composite carbon/TiO_2 electrodes

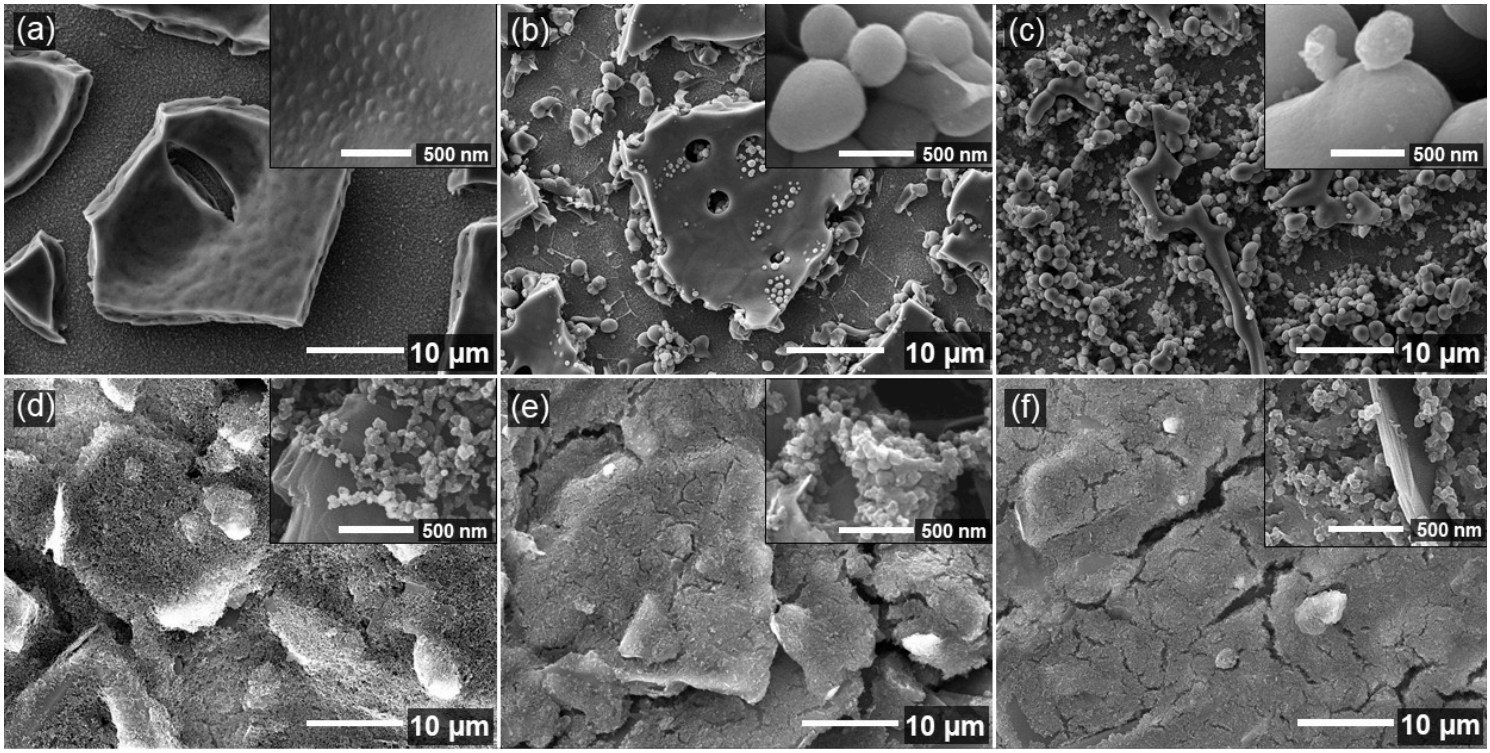


Figure 4

SEM images of sintered layers at 2 500 × magnification: (a) SG1, (b) SG2, and (c) SG3 corresponding to pure TiO_2 inorganic binders; (d) CB.G/EC reference, (e) CB.G/SG1, and (f) CB.G/SG2 corresponding to carbon/TiO_2 composite electrodes. Insets show 50 000 × magnification details.

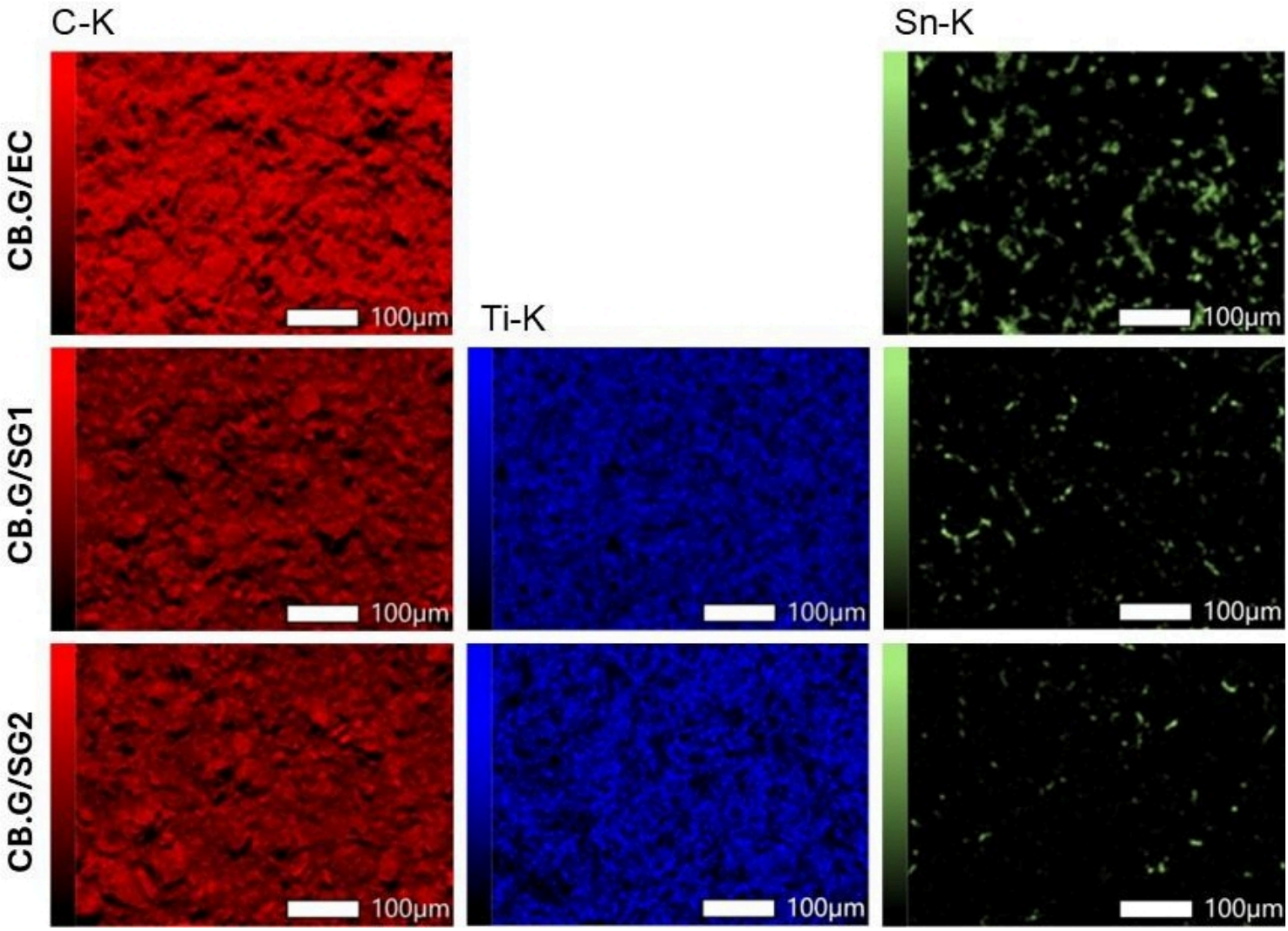


Figure 5

EDS maps illustrating the distribution of C, Ti, and Sn within carbon/TiO_2 composite layers.

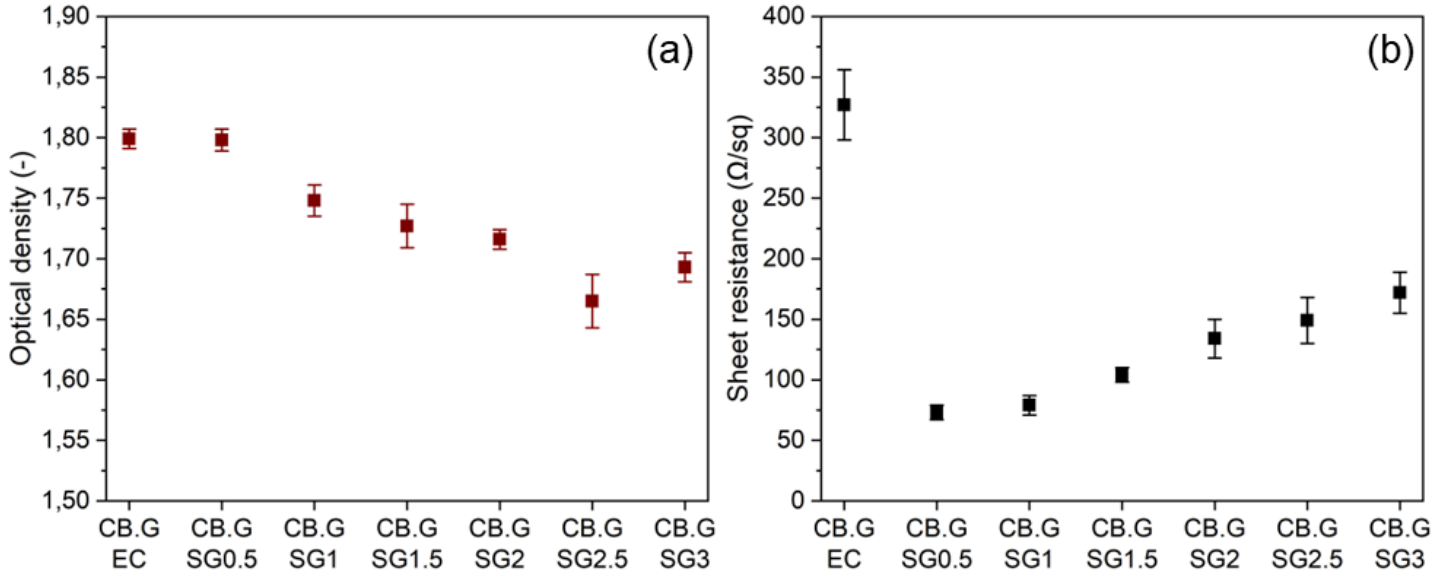


Figure 6

(a) Optical density measured in the adhesion test, (b) sheet resistance of the sintered screen-printed composite carbon/TiO_2 electrodes (CB.G/SG) and the reference CB.G/EC.

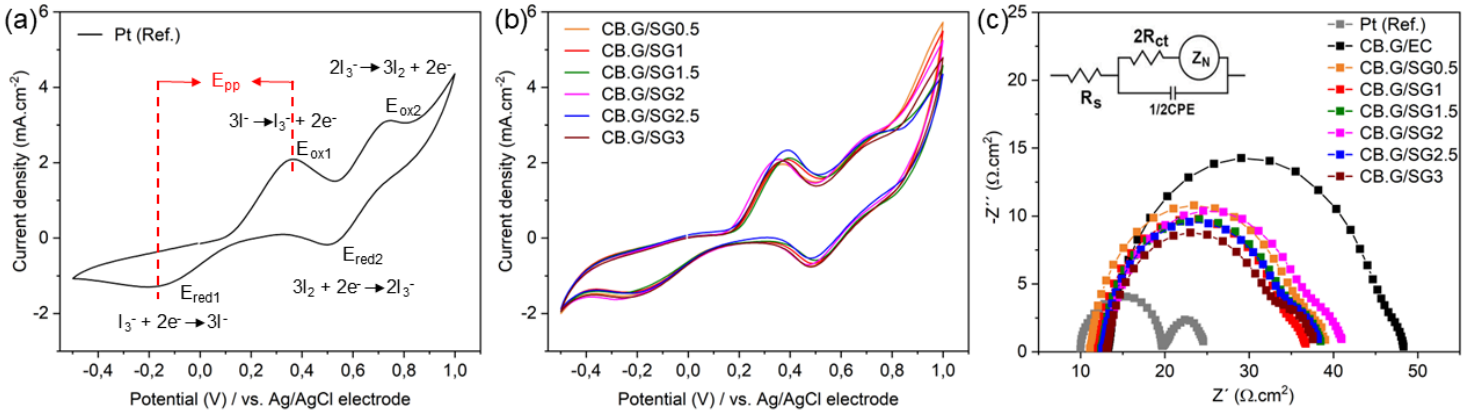


Figure 7

Cyclic voltammograms of (a) standard Pt CE, (b) composite CB.G/SG CEs with a scan rate of 100 $mV.s^{-1}$, (c) EIS Nyquist plots of the corresponding CEs.

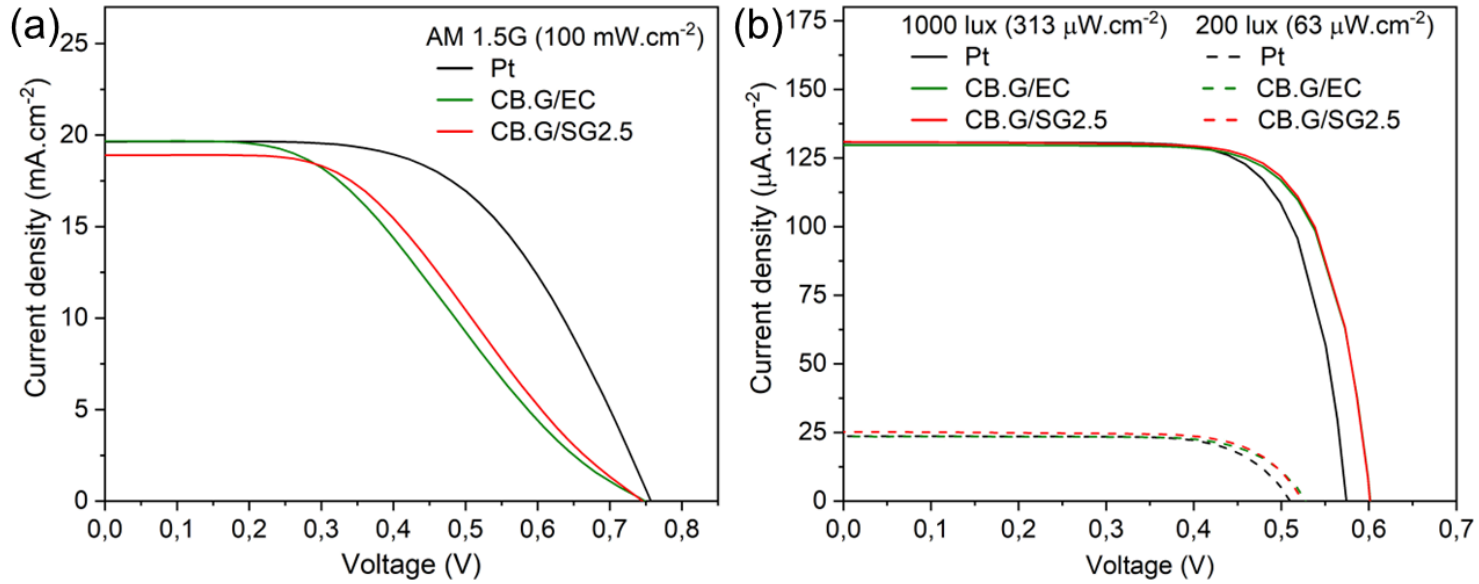


Figure 8

J-V characteristics of DSSCs measured under (a) standard illumination of 100 $mW.cm^{-2}$, (b) indoor light conditions of 1000 lux and 200 lux